



This is a repository copy of *Modified GAN-cAED to minimize risk of unintentional liver major vessels cutting by controlled segmentation using CTA/SPET-CT.*

White Rose Research Online URL for this paper:  
<https://eprints.whiterose.ac.uk/171762/>

Version: Accepted Version

---

**Article:**

Cheema, M., Nazir, A., Yang, P. [orcid.org/0000-0002-8553-7127](https://orcid.org/0000-0002-8553-7127) et al. (7 more authors) (2021) Modified GAN-cAED to minimize risk of unintentional liver major vessels cutting by controlled segmentation using CTA/SPET-CT. *IEEE Transactions on Industrial Informatics*, 17 (12). pp. 7991-8002. ISSN 1551-3203

<https://doi.org/10.1109/TII.2021.3064369>

---

© 2021 IEEE. Personal use of this material is permitted. Permission from IEEE must be obtained for all other users, including reprinting/ republishing this material for advertising or promotional purposes, creating new collective works for resale or redistribution to servers or lists, or reuse of any copyrighted components of this work in other works. Reproduced in accordance with the publisher's self-archiving policy.

**Reuse**

Items deposited in White Rose Research Online are protected by copyright, with all rights reserved unless indicated otherwise. They may be downloaded and/or printed for private study, or other acts as permitted by national copyright laws. The publisher or other rights holders may allow further reproduction and re-use of the full text version. This is indicated by the licence information on the White Rose Research Online record for the item.

**Takedown**

If you consider content in White Rose Research Online to be in breach of UK law, please notify us by emailing [eprints@whiterose.ac.uk](mailto:eprints@whiterose.ac.uk) including the URL of the record and the reason for the withdrawal request.



[eprints@whiterose.ac.uk](mailto:eprints@whiterose.ac.uk)  
<https://eprints.whiterose.ac.uk/>

# Modified GAN-cAED to Minimize Risk of Unintentional Liver Major Vessels Cutting by Controlled Segmentation Using CTA/SPET-CT

**Abstract**—This paper substantially advances upon state-of-the-art to enhance liver vessels segmentation accuracy by leveraging advantages of synthetic PET-CT (SPET-CT) images in addition to computed tomography angiography (CTA) volumes. Our setup makes a hybrid solution of modified GAN-cAED combining synthetic ability of generative adversarial network (GAN) to deliver SPET-CT images with generative ability of convolutional autoencoder (cAED) network in terms of latent learning to more refined segmentation of major liver vessels. We improve time complexity through a novel concept of controlled segmentation by introducing a threshold metric to stop segmentation up-to a desired level. The innovative concept of controlled vessel segmentation with a stopping criterion via variant threshold levels will help surgeons to avoid unintentional major blood vessels cutting, which eventually reduces the risk of excessive blood loss. Clinically, such solutions offer computer-aided liver surgeries and drug treatment evaluation in a CTA-only environment, shorten the requirement of radioactive and expensive fused PET-CT images.

**Index Terms**—Liver vessel segmentation, image synthesis, fused positron emission tomography-computed tomography (PET-CT), synthesized PET-CT (SPET-CT), liver resection.

## I. INTRODUCTION

COMPUTER tomography angiography (CTA) volumes provide vital information for computer-aided [1] liver disease-diagnosis and surgical planning. In critical cases like liver tumor resection, the medical experts must know the pathoanatomical [2] association of hepatic tumor with main blood vessels [3] to enhance the effectiveness of results. Especially, those patients who have several hepatic disorders other than liver tumors, the surgeon should eradicate the tumor cautiously with extreme care of remaining blood vessels [4] and enough liver tissue behind for adequate functionality. Due to the dual blood supply in liver, any unintentional injury to the liver tissue or associated major blood vessels during the resection leads to fatal bleeding problems. Therefore, computer aided [5] liver surgeries significantly depend upon precise vessel segmentation techniques to select the appropriate puncture pathway for minimizing unintentional cutting of liver vessels.

The accuracy of segmented vessels highly depends on properties of CTA volume like contrast, brightness, and noise presence [6]. Special care should be taken for peripheral vessels, in which contours reveal clearly. For hepatic vessels surrounding the tumors, the keen segmentation accuracy is required for completely differentiate vessels from a tumor to be removed. In case of vessel tree branches, the meeting points should be precisely marked [7]. However, vessels segmentation using only CTA volumes is still considered to be a challenging

task due to ramified nature of vessel branches, low contrasted of critical vessels as compared to surroundings, irregular vessel shapes and inherent scanner-oriented noise presence.

One possible solution to improve the results is using intensive preprocessing and post-processing of the segmented results, which, however, may impose a redundant computational cost [8]. A combined use of CTA [9] and fused PET-CT may be an alternative to complement the shortcomings of CTA volumes, i.e. difficulty to differentiate major blood vessels from liver tissue, and to improve liver vessel segmentation. The theoretical motivation of this study for offering a novel candidate in the form of CTA/fused PET-CT images is their ability to accomplish each other limitations for an enhanced liver vessels segmentation. Since last few years, a combination of CT and PET images has become a popular component of oncological analysis [10]. Anatomical details in PET image such as liver tissues are comparatively less due to a lower resolution than the CTA volume [11]. However, fused PET-CT offers cross-sectional anatomic information provided by CT and the metabolic information provided by PET. This study exploited the aforementioned trait of fused PET-CT to augment CTA vessels segmentation results.

Although the use of fused PET-CT imaging is progressively increasing yet it offers a few drawbacks. Fused PET-CT involves additional radiation disclosure in contrast to CT images. Furthermore, fused PET-CT is reasonably costly and still not popular across worldwide. The experimental significance of fused PET-CT in managing oncological applications generates a latent requirement for a substitute, cost-effective synthetic fused PET-CT (SPET-CT) imaging. Considering the rare availability of PET imaging and to avoid potential risk to patient's health due to unnecessary radiation exposure because of repetitive clinical examine, SPET-CT is an effective solution [11] for enhancing the performance of computer-aided liver surgeries. The combined use of CT and MR imaging has been extensively investigated in hepatic vessels segmentation with promising results [12]. Recently, authors in [11] have employed cross-modality CT to fused PET-CT synthesis for liver lesion segmentation. However, due to rare availability of fused PET-CT images in addition to higher radiation risk to patients, a hybrid combination of CT + fused PET-CT is still a challenge modality to overcome CT limitations for improving liver vessels segmentation

Inspired by the remarkable performance of synthetic image usage and motivated to tackle the limitations offered by the CT images, this paper aims at investigating the use of novel generative adversarial network techniques to hybrid CT and SPET-CT images for improving accuracy of liver vasculature

segmentation. Specifically, we firstly proposed a modified disco Generative Adversarial Network-convolutional Autoencoder (GAN-cAED) based model to effectively extract liver vasculatures from CTA and SPET-CT images. As shown in Fig. 1, the proposed network is composed of two components: a disco GAN to synthesize the fused PET-CT image and convolutional AED to learn the complementary features from the CTA/SPET-CT images and based on the features to produce the segmentation results. Then, we propose a new threshold metric with respect to variant dice loss function by refining the penalties for the number of under/over segmented vessels. Vessels extraction results are returned using cAED network by adjusting threshold levels for enhancing visualization of extracted vessels. Finally, the proposed technique is validated by a number of experiments to prove its efficiency on improving the visualization of segmented vessels with a required accuracy. The validation results show that the proposed method is superior to conventional intensity based models in terms of accuracy and visualization.

The main contributions of this paper are as follows:

- A novel hybrid model with generative adversarial network and autoencoder is proposed to effectively and robustly extract high quality of liver vasculatures from CTA and SPET-CT images for enhanced accuracy of liver vessels segmentation. The model enables mining latent representations of features from the CTA and SPET-CT images, further improving the segmentation performance.
- A new threshold metric with respect to variant dice loss function is introduced in the proposed model for solving the problems with elevated noise, low contrast and diverse vessel structure of CT, along with low resolution of SPET-CT. As a hybrid solution, our novel concept of variant threshold level offers a cost-effective solution in terms of stopping criterion up to desired point for controlled vessel segmentation to avoid unintentional cutting of critical (major) vessels.
- A comprehensive experimental evaluation and analysis of the proposed solution is given. The experimental results show that the proposed method is capable of delivering controlled segmentation as a cost effective solution for a given accuracy than the the conventional intensity based models [6] and recent 3D UNet based liver vessels segmentation technique [8].

In according to above advantages, our method can compute efficiently finer visualization of segmented liver vessels will boost the surgeons capabilities for effective computer-aided liver surgeries. The proposed method can proficiently build the virtual relationship of associated vessels tree with respect to the location of any required liver area. The distinctive evaluation phenomenon used in this research in terms of the threshold metric may prove to be a benchmark for concerning the quality of results.

## II. RELATED WORK

According to the latest review [13], current liver vessel segmentation techniques are generally categorized into algorithms for a deformable model, tracking-based approaches, machine

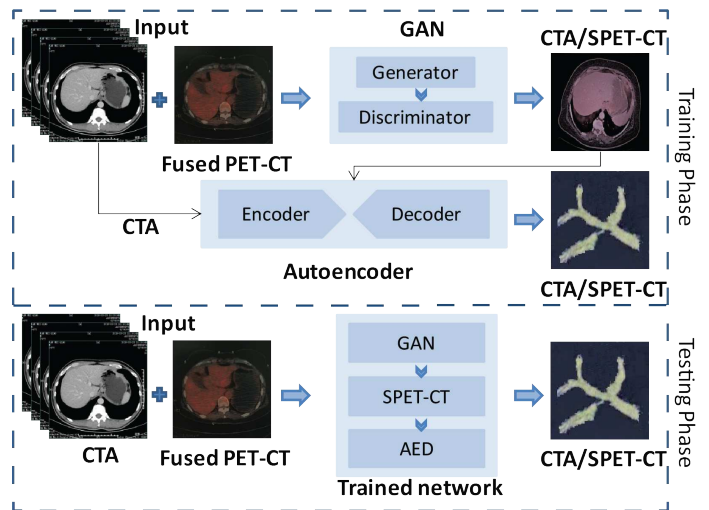


Fig. 1: The training and testing workflow of proposed network.

learning techniques, and image filtering with enhancement methods [14]. Deformable model-based algorithms closely related to level set have shown fine performance on dropping the effects of intensity contrast variations besides blood vessels. These models were typically susceptible to contour selection, initial seeds, and may generate fluctuated output into adjoining tissues for low contrast input. In tracking-based approaches, model-based algorithms are usually employed which use minimum cost path to track vessels using the predefined models [12]. These methods may prove to be error-prone for vessels with asymmetric nature especially associated with liver tumors, and hence these algorithms require post-processing as well as user assistance [15].

A review of image filtering and enhancement schemes found in [16] reveal the use of filters like Gabor, Hessian-based and Diffusion filters for vessels segmentation. These methods usually enhance vessel structure by exploiting multi-scale high order deviations and image gradients. Afterward, the enhanced vessels are extracted and segmented using context-based voting [17], graph cuts, and region-growing algorithms [18]. In machine learning-based algorithms,  $k$ -means clustering extract liver vessels and then some iterative refinements are performed for vessel reconstruction using morphological operations and linear contrast stretching [17]. The above methods have shown improved performance over state-of-the-art. However, extreme care is required to balance different parameters for devising important characteristics of liver vessels to generate an accurate segmentation of vasculature system [19].

Since past few years, deep convolutional neural networks (CNN) [20]–[25] have performed a notable enhancement regarding segmentation task for liver and retinal vessels segmentation. These networks can instinctively discover compound image attributes and merge them into hierarchical abstraction for classification and segmentation. Current CNN methods are predominantly popular for small datasets. In the case of liver vessel structure, complexity and diversity are the two main reasons for the estimated extent of segmentation results [24].

3D U-Net based method [26] has achieved a remarkable vessel segmentation in terms of accuracy and specificity

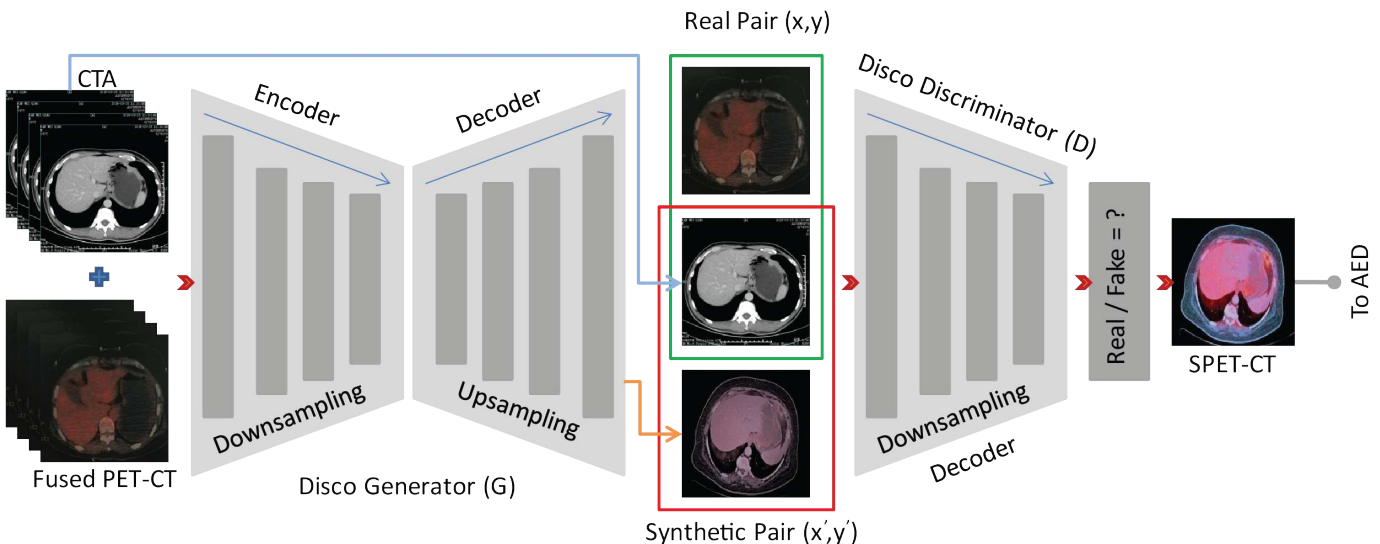


Fig. 2: The implemented GAN consists of two components. First is a disco generator ( $G$ ), which attempts to generate synthetic PET-CT image using (CTA + fused PET-CT) as an input while second is disco discriminator ( $D$ ) trained to differentiate between real  $(x, y)$  and synthetic pairs  $(\hat{x}, \hat{y})$ .  $D$  and  $G$  are neural networks where  $G$  is a disco type generator act as an adversary to  $D$ . Output of GAN i.e. SPET-CT image is feed forward to cAED.

metrics for liver vessels. However, low contrast and intensity in-homogeneity often occur in CTA volumes leads to biased segmentation results for critical vessels. Cross-modality learning with adversarial network setup of CNN is exploited to segment vessels [27]–[29]. In this setup, one network generates applicant segmentation maps by learning the latent generative representation from input image and the second one evaluates them.

Recently, a combination of CT and PET-CT images has become a popular component of oncological analysis [10], [30]. Authors in [11] used cross-modality CT to PET synthesis for liver lesions segmentation using FCN and GAN network. Although the use of PET-CT imaging is progressively increasing, PET-CT involves supplementary radiation disclosure and cost as compared to CT modality. Therefore, it is still not popular worldwide. Considering the inherent shortcomings of PET-CT and CT images, SPET-CT is an effective solution for enhancing the performance of computer-aided liver surgeries. The methods proposed in [31], [32] employed a hybrid combination of various techniques such as fuzzy connectedness and region growing to improve existing filters having an already well-known goal of achieving higher segmentation accuracies. Although, these methods have advantages in the current literature, however our work's key focus is highly varied from these mentioned papers. [Inspired from the latent capacity of learning representation of adversarial network \[11\] and to leverage the fast convergence ability of CNN, we have finely tuned mechanism for liver vasculature segmentation from CT as well as synthesized PET-CT images to deliver remarkable segmentation accuracy. The difference between our proposed solution and recent state-of-the-art is to minimize risk of unintentional vessels cutting during liver surgeries. Therefore, we have introduced novel concept of controlled segmentation using threshold metric \( \$\alpha\$ \). According to our](#)

[setup, we have used nine liver landmarks to define variant threshold levels which technically differentiate our method as compare to existing liver vessels segmentation techniques.](#)

#### A. State-of-the-Art Image Synthesis Techniques

State-of-the-art techniques for image synthesis such as atlas-based methods or simulated/physical phantoms based techniques [33] offer limited capacity in synthesizing images such as fused PET-CT. As, PET images have relatively low resolution with large anatomical and functional differences. The rapid advancement of generative adversarial networks (GANs) [11] in recent years opens a new gateway of automated image synthesis by generating realistic images with parallel implementation of generator and discriminator. The major distinctive approaches explored in current state-of-the-art for GAN-based image synthesis involve image-to-image translation [34], direct image generation [35] and image composition [36]. We have exploited the GAN-based image-to-image translation approach which aims for appearance realism by learning the style of images of the target domain.

### III. METHOD

The proposed model comprises of two core components: a GAN component to synthesize fused PET-CT images and cAED component to use CTA/SPET-CT to carry out liver vessels segmentation. The complete process is twofold described in Fig. 1. i.e. training module and a testing module. The strengths of GAN and cAED networks are combined to enhance segmentation visibility. Algorithm 1 is describing the flow of overall process. Mainly, we focus to segment critical (major) blood vessels by employing the use of realistic-looking SPET-CT images. Following subsections give details for each component of the proposed method.

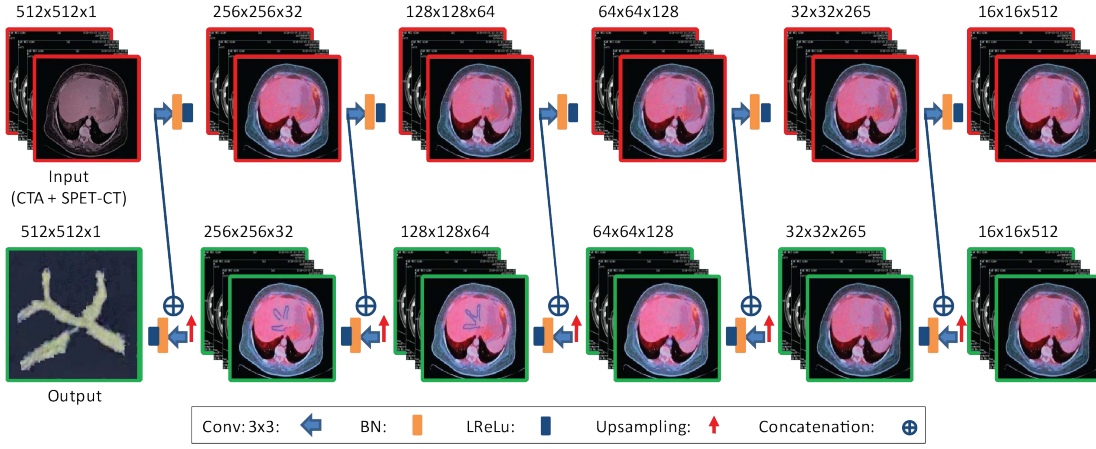


Fig. 3: Detailed architecture of cAED network. A hybrid combination of images CTA/SPET-CT is provided at input. Encoder and decoder modules contain five convolution layers for down-sampling and up-sampling respectively, followed by batch-normalization and leaky ReLU on each convolution layer.

### A. Data Preprocessing

The training module of the proposed method takes two images as input, a CTA volume and a fused PET-CT. The first step is to make alignment with respect to two types of images as CTA volume and fused PET-CT images may vary in resolution scale. We use affine transformation with linear interpolation [11] by harnessing an offset distance and voxel size of CTA volume with fused PET-CT images. For this, we denote three dimensional offset distance between CT (ct) and the fused PET-CT (pet) scan as  $(d_x, d_y, d_z)$ , three dimensional voxel size of CTA volume as  $ct\_v = (ct\_v_1, ct\_v_2, ct\_v_3)$  and voxel size of fused PET-CT scans as  $(pet\_v_1, pet\_v_2, pet\_v_3)$ .

$$\begin{bmatrix} ct/pet\_v_1 & 0 & 0 & d_x \\ 0 & ct/pet\_v_2 & 0 & d_y \\ 0 & 0 & ct/pet\_v_3 & d_z \\ 0 & 0 & 0 & 1 \end{bmatrix} \quad (1)$$

Fluoro-D-glucose (FDG) [11] is widely used radiotracer in current PET clinical practice for cancer, its uptake act as an in-vivo biomarker of glucose metabolism. Standardized uptake value (SUV) is a measured quantity that can provide insight into the histopathological nature of the tumor to assess the response of cancerous cells. In image processing SUV normalises the update values to a standard range. For measuring FDG uptake, the (SUV) [37] of PET-CT used for our setup is defined as follows:  $SUV = \frac{e}{\beta \cdot f}$ . Here, radioactivity concentration by the PET-CT scanner is denoted by  $e$  for the targeted body part,  $\beta$  is the decay-corrected quantity of inserted FDG and  $f$  is used for an associated weight of a patient. To support the proposed method for straightforwardly utilize cross-modality images of a varied range of values, we select clipping and scaling constraints to adjust PET-CT images for a range of SUV between (0 – 20) and CT images within a range of Hounsfield Units of (-160 to 240). For CT images with slice thickness below or above 5mm, we employed coordinate transform and cubic spline interpolation to adjust slice thickness of those images up to 5mm.

### Algorithm 1 GAN-cAED Learning

---

**Input:** CTA Volumes  $I^c = \{I_1^c, I_2^c, I_3^c, \dots, I_N^c\}$ , Fused PET-CT images  $I^p = \{I_1^p, I_2^p, I_3^p, \dots, I_N^p\}$ , SPET-CT images  $I^s = \{I_1^s, I_2^s, I_3^s, \dots, I_N^s\}$ , Input\_Parameters  $I^i = \{N, L, M, O\}$ , CTA/SPET – CT =  $I^c/s = [GAN(Generator(I^c, I^p) \& \& Discriminator(I^s, I^p))]$ , Iterations  $i^{th}$  to  $n^{th}$ , Threshold ( $\alpha$ );

**Output:** Learned GAN-cAED Network

$I^i \leftarrow$  Initialize Values of  $I^i = \{N, L, M, O\}$

P\_Network  $\leftarrow$  Prop\_EncoderDecoder( $I^c, I^s, I^i$ );

**for** (Encoder $_{i=1} \rightarrow$ Encoder $_{i=N}$  & & Decoder $_{i=1} \rightarrow$ Decoder $_{i=N}$ )

**do**

$L =$  Extract\_LatentInfoSPET  $\leftarrow$  Forward\_Prop( $I^i$ , Leaky ReLU $_{i=n}$ );

$M =$  Extract\_LiverVesselsSPET  $\leftarrow$  Back\_Prop( $L$ , Leaky ReLU $_{i=n}$ );

$TotalDice\_Loss = \sum \frac{1}{2} [Extracted\ Liver\ Vessels - Remaining\ Liver\ Vessels]^2$ ;

Update  $I^i$ (Dice\_Loss, Learned P\_Network);

**repeat**

**until**  $0.50 \leq \alpha \leq 0.70 \leftarrow$  Stop(M) || (Learned GAN-cAED Network=true)

**end for**

---

### B. GAN for Synthesizing Fused PET-CT

As shown in Fig. 2, the implemented GAN consists of two components. First is a generator ( $G$ ), which attempts to generate realistic looking fused PET-CT image while second is discriminator ( $D$ ) trained to differentiate between real and synthesized fused PET-CT image.  $D$  and  $G$  are neural networks where  $G$  is a disco type generator act as an adversary to  $D$ . While humans easily recognize relations between data from different image modalities without any supervision however, learning to automatically discover them is in general very stimulating. For the charge of discovering cross-modality relations from two different modalities i.e. CTA and Fused PET-CT, we have employed a modified GAN inspired from

TABLE I: Details of architectural design for convolutional autoencoder module of the proposed method with encoder and decoder layers defined separately.

Encoder			Decoder		
Layers	Details	Size:Stride	Layers	Details	Size:Stride
Input	CTA: SPET-CT	512×512×1:2	Upsampling <sub>1</sub> conv <sub>6</sub> →conv <sub>3</sub>	3×3×512 ↑ conv <sub>5</sub> →conv <sub>3</sub> ⊕ conv <sub>4</sub> →conv <sub>3</sub>	16×16×512:2
conv <sub>1</sub> →conv <sub>3</sub>	3×3×32 BN, LReLU	256×256×32:2	Upsampling <sub>2</sub> conv <sub>7</sub> →conv <sub>3</sub>	3×3×256 ↑ conv <sub>6</sub> →conv <sub>3</sub> ⊕ conv <sub>3</sub> →conv <sub>3</sub>	32×32×256:2
conv <sub>2</sub> →conv <sub>3</sub>	3×3×64 BN, LReLU	128×128×64:2	Upsampling <sub>3</sub> conv <sub>8</sub> →conv <sub>3</sub>	3×3×128 ↑ conv <sub>7</sub> →conv <sub>3</sub> ⊕ conv <sub>2</sub> →conv <sub>3</sub>	64×64×128:2
conv <sub>3</sub> →conv <sub>3</sub>	3×3×128 BN, LReLU	64×64×128:2	Upsampling <sub>4</sub> conv <sub>9</sub> →conv <sub>3</sub>	3×3×64 ↑ conv <sub>8</sub> →conv <sub>3</sub> ⊕ conv <sub>1</sub> →conv <sub>3</sub>	128×128×64:2
conv <sub>4</sub> →conv <sub>3</sub>	3×3×256 BN, LReLU	32×32×256:2	Softmax layer	-	256×256×32
conv <sub>5</sub> →conv <sub>3</sub>	3×3×512 BN, LReLU	16×16×512:2	Output	CTA/SPET-CT	512×512×1

the original disco GAN [38], [39]. The difference from the original disco GAN is that it utilized cross-domain images, we have employed it in a novel way for cross-modality image reconstruction. Unlike previous methods, our model can be trained with two sets of images without any explicit pair labels and does not require any pre-training.  $G$ 's goal is to exploit the misclassification error of  $D$ , while  $D$ 's aim is to conquer  $G$  by seeking a true representation from generated and real PET-CT images. Here,  $\hat{x}$  means the real fused PET-CT image,  $\hat{y}$  means the real CTA image and the  $G(\hat{y})$  is the generated PET-CT image. Adversarial loss of  $D$  and  $G$  is represented by the following formulation in our setup:

$$Loss_{GAN}(G, D) = \mathbb{E}_{(\hat{x}, \hat{y}) \sim pairs(\hat{x}, \hat{y})} \left[ \log D(\hat{x}, \hat{y}) \right] + \mathbb{E}_{(\hat{y}) \sim pairs(\hat{y})} \left[ \log(1 - D(\hat{y}, G(\hat{y}))) \right] \quad (2)$$

Here  $\mathbb{E}_{(\hat{x}, \hat{y}) \sim pairs(\hat{x}, \hat{y})}$  is representing estimation over the real and synthetic pairs  $(\hat{x}, \hat{y})$ . The  $G$ 's aim is to maximize  $Loss_{GAN}(G, D)$  while  $D$ 's goal is to minimize it. whereas minimizing  $Loss_{GAN}(G, D)$ , induce the generator to generate visually sharp results recent work in [40] has shown that combining Equation 3 with global loss  $L_1$  provide more consistent results. Hence, we have added a global loss  $L_1$  for more refined SPET-CT images as:

$$L_{2-recons-GAN}(G, D) = Loss_{GAN}(G, D) + \alpha \mathbb{E}_{(\hat{x}, \hat{y}) \sim pairs(\hat{x}, \hat{y})} \left[ \|\hat{y} - G(\hat{y})\| \right] \quad (3)$$

Where  $\alpha$  is the threshold loss to balance the two losses of generator and discriminator.

### C. cAED as a Generative Model for Segmenting Liver Vessels

Convolutional autoencoder used in this research, is a particular type of self-supervised feed forward convolutional neural network [13] where the input images (CTA+SPET-CT) is compressed into a lower-dimensional latent-space representation and then reconstruct the output from this representation in the form of CTA/SPET-CT images with marked segmented vessels.

The input (CTA+SPET-CT) passes through the encoder  $X$ , which is a fully convolutional neural network having, five  $3 \times 3$  convolution layers for down-sampling followed by batch-normalization and leaky ReLU as an activation function. Table I is describing the detailed architecture of our cAED network. Encoder  $X$  maps an input image  $M$  to latent representation  $W = X(M)$ . The decoder  $Y$  has a similar CNN structure by having five  $3 \times 3$  convolution layers for up-sampling followed by Batch-Normalization and Leaky ReLU. Decoder  $Y$  maps  $W$  to an output aims to be an image CTA/SPET-CT with segmented vessels, further details of the architectural design are represented in Fig. 3.

Along with reducing the dimensionality of input data, cAED reconstructs an output using the learned latent representation  $W$ . For which the decoder as a second model takes input in the form of a combination of the real CTA and generated PET-CT image, while its output is the vessel segmentation result. We have trained the convolutional autoencoder into a training set of input images (CTA+SPET-CT), in order to reduce a reconstruction loss  $R_{Loss}(X, Y)$  to determine probability distributions  $X(M|W)$ ,  $Y(W|M)$ . To achieve proper abstraction from convolutional autoencoder, several types of regularization are employed e.g. minimizing  $R_{Loss}(X, Y)$  to fulfill the goal of providing new fundamentals close to the original input data [41]. Thus, the proposed setup efficiently utilize adversarial network synthesis ability along with the generative power of convolutional autoencoder network in terms of latent learning process to segment more refined liver vessels.

We have utilized gradient descent to perform training with the gradients estimated by standard back-propagation [42]. This is accomplished by maximizing the following loss:

$$R_{Loss}(X, Y) = \mathbb{E}_{W \sim Y(W)} \left[ \log(X_W(W)) \right] + \mathbb{E}_{M \sim Y(data(M))} \left[ \log(1 - X_W(X(W/M))) \right] \quad (4)$$

Now the complete loss of convolutional autoencoder along

TABLE II: Experimental results of various threshold ( $\alpha$ ) levels ( $0.50 \leq \alpha \leq 0.70$ ) on controlled vessels segmentation in terms of seven metrics.

Threshold ( $\alpha$ )	Sensitivity(%)	Specificity(%)	Accuracy(%)	Dice(%)	Recog Rate(%)	Overlap measure(%)	Avg distance(mm)
$\alpha = 0.50$	84.4±0.4	96.7±0.7	96.8±0.3	91.65±0.3	95.92±0.15	66.5±0.24	1.37±0.85
$\alpha = 0.55$	86.3±0.2	98.5±0.6	97.9±0.4	92.40±0.4	96.16±0.54	68.2±0.45	2.01±1.45
$\alpha = 0.60$	<b>89.1±0.5</b>	<b>99.9±0.6</b>	<b>99.8±0.1</b>	<b>95.30±0.6</b>	<b>97.41±0.25</b>	<b>69.0±0.34</b>	<b>2.50±1.61</b>
$\alpha = 0.65$	86.5±0.6	94.5±0.4	95.4±0.8	93.35±0.8	94.19±0.17	63.8±0.63	1.21±1.23
$\alpha = 0.70$	87.6±0.4	95.9±0.2	94.6±0.9	92.16±0.9	93.25±0.46	62.9±0.45	1.03±1.25

with GAN network loss is calculated as follows:

$$R_{Loss_{comb}}(X, Y, GAN) = R_{Loss}(X, Y) + \eta Loss_{op-GAN}(G, D) \quad (5)$$

Here,  $\eta$  represents the importance of weights for the two losses. From the above relation, it is obvious that both sub-tasks are profoundly interrelated. As a consequence, cAED also attains payback when the GAN produces realistic SPET-CT images. A schematic demonstration of the complete convolutional autoencoder module is illustrated in Fig. 3.

#### D. Threshold ( $\alpha$ ) for Controlled Segmentation

To avoid mislabeled vessel branches caused by biased classification due to unlabeled foreground (vessels) and background (liver) classes, we have introduced a threshold metric to establish controlled segmentation.

For defining a threshold ( $\alpha$ ) according to our setup we have used nine liver anatomical landmarks [17]. Using landmarks, it is deduced that the portal vein and hepatic artery deliver blood to the liver by dividing into branches of a sinusoid. Sinusoids join to formulate hepatic vein to drain the liver. Usually, in CT images, sinusoids are invisible, so portal and hepatic vessels are visually alienated vasculature [17]. Based on the anatomical landmark hierarchy, our proposed method segment liver vasculature globally i.e. on the branch level (BL), for controlled segmentation using a threshold ( $\alpha$ ) as:

$$Threshold(\alpha) = [CV_{i,j,k} \cup BL] \quad (6)$$

The connectivity measures all potential paths of a vessel ( $i, j, k$ ) in three dimensions to extend a tubular structure. In other words, we can measure curvature  $\theta$ , length of a vessel  $l$ , diameter  $r$  with respect to each direction ( $e_1$  for  $l$ , and  $e_2$  for  $r$ ), using connectivity between vessels of the segmented tree. Hence connectivity  $CV_{(i,j,k)}$  of tree vessels in three dimensions is defined as:

$$CV_{(i,j,k)} = \begin{cases} 1 & \text{if } f \leq 0.9 \\ \exp(-\frac{r^2}{e_1^2})\exp(-\frac{l^2}{e_2^2}) & \text{if } f > 0.9, -\frac{\pi}{0.5} \leq \theta \leq \frac{\pi}{0.5} \\ 0 & \text{if } \text{others} \end{cases} \quad (7)$$

Branch level (BL) on a threshold is the recognition rate of vessels and it is measured as:

$$BL_{(i,j,k)} = \begin{cases} LHV, MHV, RHV & \text{if } cv_{(i,j,k)} \leq 0.70 \\ LPV, MPV, RPV & \text{if } cv_{(i,j,k)} \geq 0.50 \\ \text{others} & \text{if } cv_{(i,j,k)} < 0.50 \end{cases} \quad (8)$$

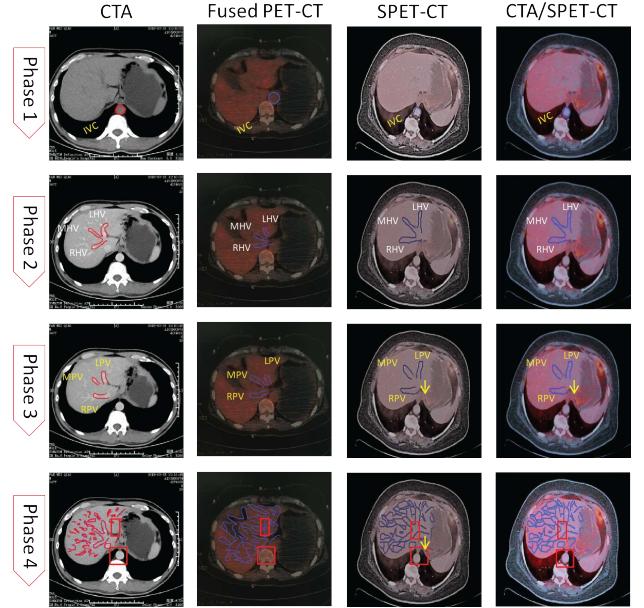


Fig. 4: Qualitative results during phase 1 to 4 using CTA, Fused PET-CT, SEPT-CT, and CTA/SPET-CT data.

Hence using connectivity  $CV_{(i,j,k)}$  and branch level  $BL_{(i,j,k)}$  the threshold ( $\alpha$ ) values vary from 0.50 – 0.70. Using this varied value we have defined criteria for controlled segmentation. Our approach detects critical vessels i.e left, middle, and right hepatic arteries and portal veins (LHA, MHA, RHA, LPV, MPV, and RPV) for the defined levels of threshold ( $0.50 \leq \alpha \leq 0.70$ ) illustrated in Fig. 5. We have redefined Dice Similarity Coefficient (DSC) to evaluate segmentation accuracy of our approach. Generally, DSC is defined as:

$$DSC_{v_1}(E, R) = \frac{(E \cap R)}{(E \cap R) \pm 0.5(|E - R| + |E + R|)} \quad (9)$$

Where  $E$  is the estimated position of segmented vessels and  $R$  is the ground truth position of estimated vessels tree. Introducing  $\alpha$  in  $DSC_{v_2}$  gives us a variant of  $DSC_{v_1}$  using  $\alpha$  values i.e. ( $0.50 \leq \alpha \leq 0.70$ ). Variant  $DSC_{v_2}$  is defined by adding  $\alpha$  for estimated tree values  $E_i$  and ground truth values  $R_i$  for foreground ( $E_{1i}, R_{1i}$ ) and background ( $E_{2i}, R_{2i}$ ) classes as:

$$DSC_{v_2}(E, R, \alpha) = \frac{\sum_{i=1}^n E_{1i}R_{1i}}{\sum_{i=1}^n E_{1i}R_{1i} + 0.5\alpha \sum_{i=0}^N (E_{1i}R_{2i} + E_{2i}R_{1i})} \quad (10)$$

The variant of  $DSC_{v_2}$  in addition to refined threshold help us to detect critical vessels and ignore non-critical vessels to enable

TABLE III: Quantitative results of proposed method with three levels of  $SUV$  (high, medium, and low) for different formations in terms of mean absolute error (MAE) and peak-signal-to-noise-ratio (PSNR).

Our Method (Variants)	High		Medium		Low		Average	
	MAE	PSNR	MAE	PSNR	MAE	PSNR	MAE	PSNR
$\alpha_{0.55}$ (GAN+cAED)	1.40±0.75	22.0±0.48	0.14±0.03	33.3±1.70	0.80±0.01	38.2±1.02	0.718±0.216	31.1663±1.064
$\alpha_{0.60}$ (GAN+cAED)	1.29±0.74	20.1±0.65	0.12±0.01	35.1±1.60	0.65±0.03	38.1±1.35	0.686±0.260	31.100±1.200
$\alpha_{0.65}$ (GAN+cAED)	1.45±0.40	23.0±0.49	0.13±0.04	34.6±1.60	0.70±0.05	40.1±1.32	0.716±0.116	32.067±1.136
GAN-U-Net Variant	1.35±0.50	21.5±0.42	0.12±0.02	36.7±1.50	0.90±0.03	41.0±1.89	0.719±0.181	33.134±1.273
GAN-FCN Variant	1.49±0.42	21.9±0.57	0.17±0.01	32.7±1.30	0.81±0.06	42.7±1.25	0.822±0.162	32.413±1.041
cAED-Loss-Variant <sub>1</sub>	1.38±0.30	22.8±0.65	0.16±0.05	34.9±1.35	0.95±0.07	40.3±1.35	0.831±0.143	32.614±1.116
cAED-Loss-Variant <sub>2</sub>	1.35±0.25	20.9±0.70	0.15±0.07	38.3±1.45	0.11±0.03	44.1±1.42	0.539±0.121	34.015±1.201

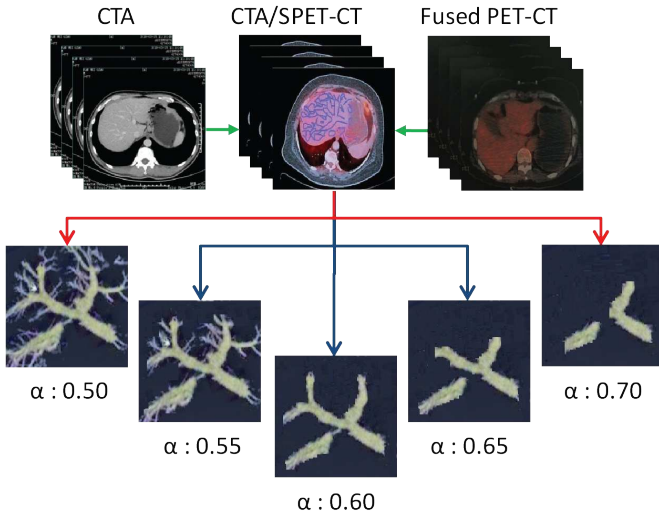


Fig. 5: Threshold ( $\alpha$ ) impact on controlled vessels segmentation.  $\alpha=0.50$  and  $\alpha=0.70$  shows over-segmentation and under-segmentation respectively whereas  $\alpha=0.60$  is best suited for concrete and compact vessels tree segmentation.

the proposed method efficiently segment vessels by reducing the time complexity.

#### IV. EVALUATIONS AND DISCUSSIONS

To evaluate the qualitative and quantitative performance of the proposed approach, we carried out several sets of experiments using visual and statistical comparisons based on threshold ( $\alpha$ ) variants.

##### A. Datasets Description

To express the achievability of learning compact visualization from large-scale 3D volumetric data, the proposed technique has been assessed on two clinical datasets. First, 150 CTA volumes collected in the year 2018 from co-operated hospital<sup>1</sup>. The type of CTA volume was contrast enhanced with axial views of abdomen parts. Each CTA volume is comprised of four phases i.e. arterial, portal, venous, and equilibrium phase. The quantity of a voxel of CTA dataset was approximately  $350 \times 300 \times 350$  with voxel spacing from  $(0.85mm, 0.75mm, 0.85mm)$  to  $(0.95mm, 1.0mm, 0.95mm)$  having slice thickness of  $5mm$ .

<sup>1</sup>Institute of Diagnostic and Interventional Radiology, Shanghai Jiao Tong University Affiliated Sixth People's Hospital, Shanghai 200233, China

Second is a fused PET-CT dataset comprises of 150 scans with a slice thickness of  $4mm$  and  $3mm$  as pixel spacing.

##### B. Implementation Details

The ratio for training, testing, and validation for CTA and fused PET-CT datasets comprises  $(3 : 1 : 1)$ . Our method utilized paired images of CTA + fused PET-CT for training as well as testing. The training time was about 60 hours with GPU of NVIDIA GeForce GTX Titan and 2.70 GHz Intel Xeon E5-2680 CPU. It takes around 2 minutes to segment liver vessels from CTA/SPET-CT image on a trained GAN-cAED network. We have obtained the manually labeled ground truth of  $(30 \text{ CTA} + 30 \text{ fused PET-CT scans})$ . It cost around 30 days (5 hours per day) to manually label our required data by two medical experts from the same cooperated hospital. Final segmentation results are cross verified from the experts to clinically validate the obtained accuracy.

##### C. Qualitative Evaluation

For qualitative results, we have presented a visual evaluation of the proposed approach in Fig. 4. This pictorial illustration is showing our synthetically generated images and final segmentation results. From left to right, column 1 to column 4, four phases of CTA and fused PET-CT images are represented while top to bottom rows are showing the mechanism of the proposed approach to synthesize SPET-CT image. Results to segment liver vessels form CTA/SPETCT images are presented in the last row. The initial segmented result of the hepatic vasculature is morphologically not as clear between hepatic vein and portal vein because at this stage i.e. third row-phase three, the system does not add refinement by addition of CTA/SPET-CT images. After segmenting vessels from CTA/SPET-CT image at last row-phase four, we can see the concrete vessels segmentation results showing six critical identified components i.e. left hepatic, right hepatic, middle hepatic, and left portal, middle portal, and right portal veins. The hepatic artery and portal vein branches are marked on the visual results according to their actual anatomical location in the liver.

##### D. Threshold ( $\alpha$ ) Impact on Controlled Vessels Segmentation

The impact of various threshold values on quality as well as applicability of our novel concept i.e. controlled segmentation are illustrated in Fig. 5. Vessels segmentation results are retuned by threshold levels  $(0.50 \leq \alpha \leq 0.70)$  for enhancing

visualization of critical (major) vessels and to ignore non-critical (thin) vessels. As shown in Fig. 5, variants of threshold levels will provide an opportunity to surgeons for controlled segmentation up to the desired level. In addition, it will offer a stopping criterion for vessels segmentation with cost-effective solution. In the given dataset,  $\alpha$  value at 0.5 shows over-segmentation results as during liver ablation, surgeons have to take care of blood vessels which are most critical with respect to the source of major blood supply, hence over-segmentation may induce time and resource complexity. While  $\alpha = 0.70$  in Fig. 5 shows under-segmentation results for vessels tree generation from CTA/SPET-CT, which is again will provide incomplete details for accurate liver surgical treatments. Therefore, in the given dataset, our proposed approach defined an optimal threshold value at 0.6 for concrete and compact vessels tree segmentation as a cost-effective solution. Fig. 6 provided more qualitative results to visually demonstrate the accuracy of proposed method.

### E. Quantitative Evaluation

As described in Table II, we have used following seven metrics i.e. sensitivity, specificity, accuracy, dice, branch level (recog. rate), overlap measure, and avg distance to measure the performance of this research quantitatively with respect to  $\alpha$  levels. In our setup, sensitivity and specificity are the metrics to indicate the amount of properly segmented vessels for true positive and true negative classes.

The branch-level (recong. rate) is defined as the ratio of the number of correctly segmented vessels branches to the portal/hepatic veins divided by a total number of assembled branches of major vessels. Table II describes the values of the threshold metric from a range of 0.50 to 0.70. It is deduced that at  $\alpha = 0.60$ , the proposed system shows the best results of sensitivity (%) =  $89.1 \pm 0.5$ , specificity (%) =  $99.9 \pm 0.6$ , accuracy (%) =  $99.8 \pm 0.1$ , DSC (%) =  $95.30 \pm 0.6$ , branch level (recog. Rate %) =  $97.41 \pm 0.25$ , overlap measure (%) =  $69.0 \pm 0.34$ , and average distance (mm) =  $2.50 \pm 1.61$ . The best values of sensitivity, specificity and accuracy at  $\alpha = 0.60$  for our technique are also illustrated in Fig. 7a.

### F. Discussion on Various Combination of the Proposed Method w.r.t SUV Range

As discussed in Table III and illustrated in Fig. 7b, we have accomplished a various combinations of the proposed approach with the three levels of SUV range i.e high (larger than 2.5), medium (approx 1.5) and low (less than 0.9). On all these three levels we have calculated the mean absolute error (MAE) and peak-signal-to-noise-ratio (PSNR).

From Table III, we can deduce that variants of GAN network i.e. FCN [11] as a generator in GAN-FCN and U-Net [26] as a generator in GAN-U-Net, U-Net convergence is better to give appropriate reconstruction results and synthesize enhanced quality SPET having lower values of PSNR and MAE at high SUV levels. From variants of convolutional autoencoder network with respect to simple dice loss (cAED\_Loss  $v_1$ ) and variant dice loss in addition to threshold metric (cAED\_Loss  $v_2$ ), we have achieved better

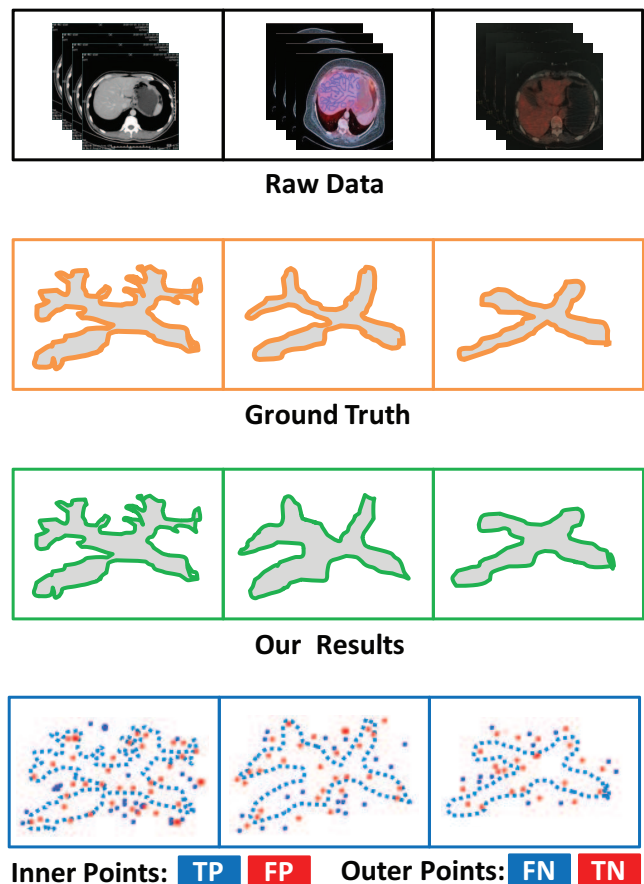


Fig. 6: Qualitative results to show the comparison of gold standard ground truth and obtained segmentation. The blue dots inside the segmented liver vasculature are showing true positive (TP) for our model means correctly segmented; however blue dots outside the boundary of liver vasculature are labeled as false positive (FP) means incorrectly segmented. On the contrary, a true negative (TN) is a case indicating red dots outside the liver vasculature boundary showing correctly not segmented, red dots inside the segmented liver vasculature boundary are false negative (FN) in the case of incorrect segmentation.

TABLE IV: Experimental results on various formations of the proposed technique for optimal value of  $\alpha = 0.60$ .

P.Network variants @( $\alpha = 0.60$ )	Accuracy (%)	Sensitivity (%)	Specificity (%)
$v_1$ (cAED_loss $_1$ +GAN-U-NET)	96.6 $\pm$ 0.33	66.8 $\pm$ 0.30	95.1 $\pm$ 0.63
$v_2$ (cAED_loss $_1$ +GAN-FCN)	97.7 $\pm$ 0.54	85.8 $\pm$ 0.45	96.8 $\pm$ 0.14
$v_3$ (cAED_loss $_2$ +GAN-U-NET)	<b>99.8<math>\pm</math>0.10</b>	<b>89.2<math>\pm</math>0.32</b>	<b>99.9<math>\pm</math>0.25</b>
$v_4$ (cAED_loss $_2$ +GAN-FCN)	97.4 $\pm$ 0.76	85.1 $\pm$ 0.76	95.8 $\pm$ 0.65

results for (cAED\_Loss  $v_2$ ) in terms of lower values of MAE and PSNR. Whereas, among variants of proposed method with respect to three threshold levels i.e. [ $\alpha = 0.55$ (GAN+cAED),  $\alpha = 0.60$ (GAN+cAED), and  $\alpha = 0.65$ (GAN+cAED)],  $\alpha = 0.60$ (GAN+cAED) gives the best performance for high SUV on values of MAE =  $0.65 \pm 0.03$ , and PSNR =  $38.1 \pm 1.35$ . Table IV shows another set of experiments on combining various formations of the proposed technique by keeping

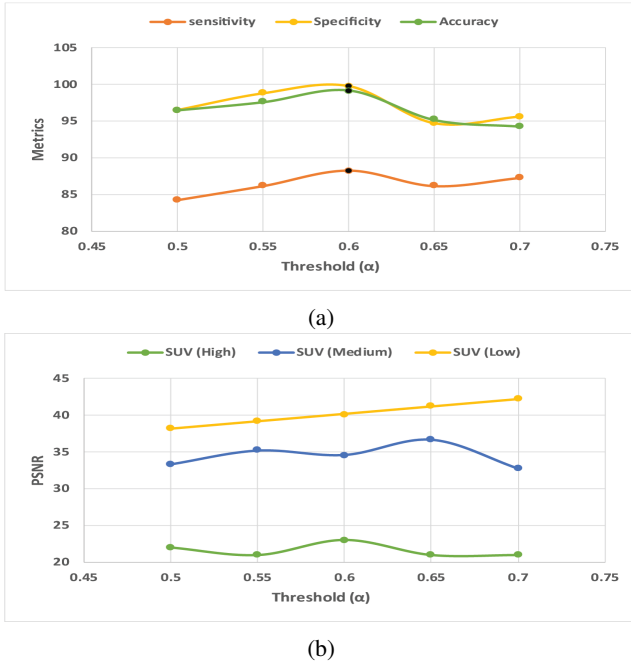


Fig. 7: (a) Quantitative evaluation in terms of sensitivity, specificity, and accuracy. The black dots with highest metrics values at  $\alpha = 0.60$  are showing an optimal value of threshold. (b) Quantitative evaluation of three levels of *SUV* range in terms of peak-signal-to-noise-ratio (PSNR).

threshold consistent at  $\alpha = 0,60$ . We have achieved the best results at  $v_3(\text{cAED } \text{loss}_2 + \text{GAN-U-NET})$  for which we have use variant DSC in addition to threshold and U-Net as a generator in GAN. We have described various levels

TABLE V: Comparison of our method with six state-of-the-art approaches w.r.t dice (%), accuracy (%), and sensitivity (%).

Methods	Dice(%)	Accuracy(%)	Sensitivity(%)
Chi et al. [17]	72.5 $\pm$ 7.4	97.5 $\pm$ 0.1	79.2 $\pm$ 8.3
Lu et al. [4]	76.6 $\pm$ 7.2	90.6 $\pm$ 0.4	77.1 $\pm$ 7.1
Zeng et al. [43]	79.9 $\pm$ 3.5	97.7 $\pm$ 0.3	85.7 $\pm$ 7.7*
Zeng et al. [6]	84.1 $\pm$ 3.3	97.8 $\pm$ 0.6*	83.1 $\pm$ 4.5
Huang et al. [8]	92.5 $\pm$ 7.2*	98.7 $\pm$ 0.2*	85.6 $\pm$ 6.8
Ban et al. [11]	93.6 $\pm$ 2.9*	96.4 $\pm$ 0.5	85.9 $\pm$ 3.1*
<b>Our Method</b>	<b>94.9<math>\pm</math>0.4</b>	<b>99.8<math>\pm</math>0.3</b>	<b>87.3<math>\pm</math>2.6</b>

$P < 0.05$ , \* derived for a paired t-test shows statistically significance difference.

of threshold with respect to sensitivity and specificity in receiver operating characteristics (ROC) curves with respect to statistical results obtained from Table IV as shown in the Fig. 8.

Additionally, we have conducted experiments for the various level of threshold with respect to following four metrics. i.e. Root Mean Square (RMS) symmetric surface distance (mm), average symmetric surface distance (mm), relative absolute volume difference (%), volumetric overlap error (%). Table VI is showing the obtained results with respect to five threshold levels.

TABLE VI: Experimental results of the proposed method based on  $\alpha = 0.50$  to  $\alpha = 0.70$  using VOE (%), RAVD (%), ASSD (mm), and RMS-SSD (mm).

Levels ( $\alpha$ )	VOE (%)	RAVD (%)	ASSD (mm)	RMS-SSD (mm)
$\alpha = 0.50$	9.84	6.75	0.59	0.68
$\alpha = 0.55$	6.53	5.52	0.45	0.59
$\alpha = 0.60$	<b>5.52</b>	<b>4.23</b>	<b>0.23</b>	<b>0.35</b>
$\alpha = 0.65$	6.19	5.98	0.34	0.45
$\alpha = 0.70$	8.32	6.95	0.49	0.57
Avg values	7.28	5.88	0.42	0.52

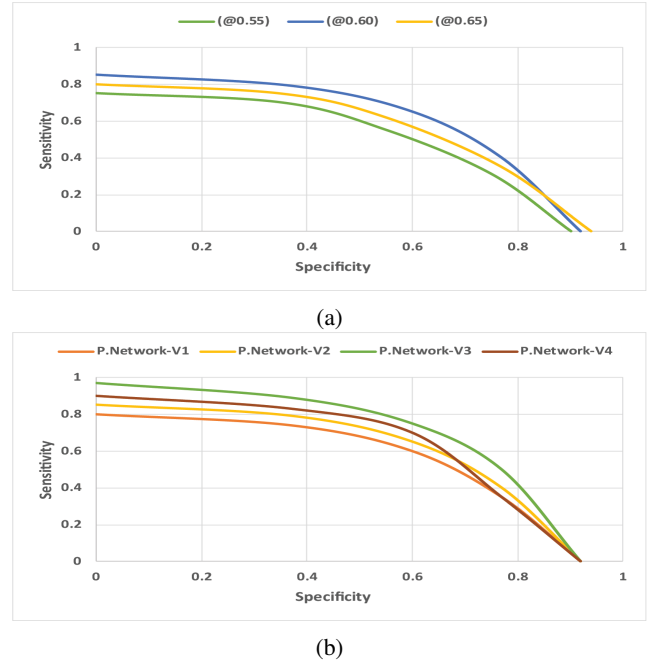


Fig. 8: (a) Receiver operator curves (ROC) for various levels of threshold metric ( $\alpha$ ) with respect to sensitivity and specificity.  $\alpha$  value @ 0.55 shows under-segmentation represented by green curve with area under the ROC Curve (AUC) = 0.75,  $\alpha$  @ 0.65 in yellow curve are over-segmentation having AUC = 0.8 and  $\alpha$  @ 0.60 in blue curve is representing best suited threshold level with AUC = 0.90 for an optimal vessels tree generation. (b) Quantitative evaluation of proposed method on set of experiments combining various formations of the proposed technique with respect to threshold values for ROC curves. Four formations of the proposed technique includes  $v_1(\text{cAED } \text{loss}_1 + \text{GAN-U-NET})$  as *P.NetworkV1* in orange curve,  $v_2(\text{cAED } \text{loss}_1 + \text{GAN-FCN})$  as *P.Networkv2* in yellow curve,  $v_3(\text{cAED } \text{loss}_2 + \text{GAN-U-NET})$  as *P.Networkv3* in green curve,  $v_4(\text{cAED } \text{loss}_2 + \text{GAN-FCN})$  as *P.Networkv4* in brown curve with respect to sensitivity, and specificity.  $V_3(\text{cAED } \text{loss}_2 + \text{GAN-U-NET})$  shows the best performance with AUC = 0.92 represented by green curve.

### G. Comparison with State-of-the-Art Methods

Table V describes the comparison of the proposed method with six state-of-the-art liver vessels segmentation approaches. The methods like Huang et al. [8] has used 3D-U-Net, Ben et al. [11] employed GAN-FCN to use cross-modality CT to PET images, Chi et al. [17] implement context-based voting,

Lu et al. [4] make use of a variational level set method, Zeng et al. have applied oriented flux symmetry with graph cuts in [43] and centerline constraint in addition to intensity model for [6].

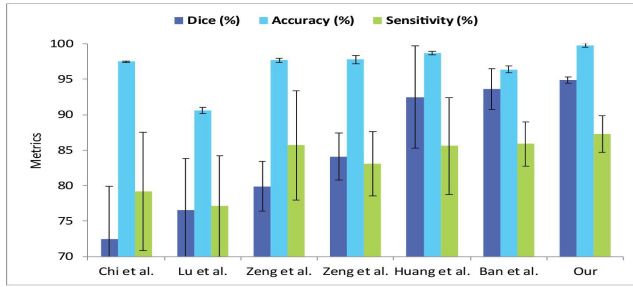


Fig. 9: Comparison of the proposed method with six state-of-the-art liver vessels segmentation approaches.

We have carried out performance evaluation using dice (%), accuracy (%), and sensitivity (%) of segmented liver vessels. It is revealed from the Fig. 9 that we have achieved improved results on all the mentioned existing techniques in terms of dice (%)=94.9±0.4, accuracy (%)=99.8±0.3, and sensitivity (%)=87.3±2.6. For testing the significance of differences between the results of comparison methods, we have computed the p-value using the paired t-test (two-sample t-test) with significance level of p at 0.05. Although the recent 3D U-Net based liver vessels segmentation [8] and intensity based models [6] generate liver vasculature system with accuracy up to approximately 97%, however, our method gives a novel idea of controlled segmentation by employing threshold levels for a cost-effective medical solution. Fig. 9 illustrates that obtained results are comparable to the Huang et al. [8] still, we have achieved enhanced accuracy with controlled segmentation using fusion of (CTA + SPET-CT images) to make fine refinements in vessels segmentation accuracy and visualization which differentiates the proposed method from existing liver vessel segmentation methods. This study solely aims to minimize risk of unintentional liver major vessels cutting by controlled segmentation using CTA/SPET-CT. Tumor structure detection and quantifying its locality with respect to critical blood vessels can be an extension of this work.

## V. CONCLUSION

The three-dimensional CTA volumes provides vital information for computer-aided liver diagnosis and surgical planning. The information of comparative position of diseased area with associated vessel branches may enhance the effectiveness of liver ablation and resection results. Inspired by the remarkable performance of synthetic images usage and also motivated to tackle the limitation offered by the current CT images, we propose a novel GAN-cAED model to extract liver vasculatures from a hybrid combination of CTA/SPET-CT images. Vessel segmentation results are retuned by proposing variant threshold levels with respect to dice loss function for enhancing visualization of critical (major) blood vessels and to ignore non-critical (thin) vessels for avoiding unintentional

cutting to minimize the risk of excessive blood loss. Visually enhanced segmented vessels will boost the surgeon's capabilities in computer-aided liver surgeries and drug treatment. The proposed method will efficiently guide surgeon's to estimate the comparative position of the diseased area with associated major blood vessels in a CTA-only environment with least requirement of radioactive PET scans.

## REFERENCES

- [1] M. Marsousi, K. Plataniotis, and S. Stergiopoulos, "Computer-assisted 3-d ultrasound probe placement for emergency healthcare applications," *IEEE Transactions on Industrial Informatics*, vol. 12, no. 4, pp. 1380–1391, Aug 2016.
- [2] M. A. Simo, P. Neto, and O. Gibaru, "Unsupervised gesture segmentation by motion detection of a real-time data stream," *IEEE Transactions on Industrial Informatics*, vol. 13, no. 2, pp. 473–481, April 2017.
- [3] N. Lv, C. Chen, T. Qiu, and A. K. Sangaiah, "Deep learning and superpixel feature extraction based on contractive autoencoder for change detection in sar images," *IEEE Transactions on Industrial Informatics*, vol. 14, no. 12, pp. 5530–5538, Dec 2018.
- [4] S. Lu, H. Huang, P. Liang, G. Chen, and L. Xiao, "Hepatic vessel segmentation using variational level set combined with non-local robust statistics," *Magnetic Resonance Imaging*, vol. 36, pp. 180–186, 2017.
- [5] G. S. Aujla, R. Chaudhary, K. Kaur, S. Garg, N. Kumar, and R. Ranjan, "Safe: Sdn-assisted framework for edgecloud interplay in secure healthcare ecosystem," *IEEE Transactions on Industrial Informatics*, vol. 15, no. 1, pp. 469–480, Jan 2019.
- [6] Y.-z. Zeng, Y.-q. Zhao, S.-h. Liao, M. Liao, Y. Chen, and X.-y. Liu, "Liver vessel segmentation based on centerline constraint and intensity model," *Biomedical Signal Processing and Control*, vol. 45, pp. 192–201, 2018.
- [7] B. Lei, P. Yang, T. Wang, S. Chen, and D. Ni, "Relational-regularized discriminative sparse learning for alzheimer's disease diagnosis," *IEEE Trans. Cybern.*, vol. 47, no. 4, pp. 1102–1113, 2017.
- [8] Q. Huang, J. Sun, H. Ding, X. Wang, and G. Wang, "Robust liver vessel extraction using 3D U-Net with variant dice loss function," *Computers in Biology and Medicine*, vol. 101, pp. 153–162, 2018.
- [9] Y. Wang, G. Ma, L. An, F. Shi, P. Zhang, D. S. Lalush, X. Wu, Y. Pu, J. Zhou, and D. Shen, "Semisupervised triple dictionary learning for standard-dose PET image prediction using low-dose PET and multimodal MRI," *IEEE Trans. Biomed. Eng.*, vol. 64, no. 3, pp. 569–579, 2017.
- [10] M. Filipović, É. Barat, T. Dautremer, C. Comtat, and S. Stute, "PET reconstruction of the posterior image probability, including multimodal images," *IEEE Trans. Med. Imag.*, pp. 1–13, 2018.
- [11] A. Ben-Cohen, E. Klang, S. P. Raskin, S. Soffer, S. Ben-Haim, E. Konen, M. M. Amitai, and H. Greenspan, "Cross-modality synthesis from CT to PET using FCN and GAN networks for improved automated lesion detection," *Engineering Applications of Artificial Intelligence*, vol. 78, pp. 186–194, 2019.
- [12] S. Cetin and G. Unal, "A higher-order tensor vessel tractography for segmentation of vascular structures," *IEEE Trans. Med. Imag.*, vol. 34, no. 10, pp. 2172–2185, 2015.
- [13] S. Moccia, E. De Momi, S. El Hadji, and L. S. Mattos, "Blood vessel segmentation algorithms – Review of methods, datasets and evaluation metrics," *Computer Methods and Programs in Biomedicine*, vol. 158, pp. 71–91, 2018.
- [14] A. Nazir, M. N. Cheema, B. Sheng, P. Li, J. Kim, and T. Y. Lee, "Living donor-recipient pair matching for liver transplant via ternary tree representation with cascade incremental learning," *IEEE Transactions on Biomedical Engineering*, pp. 1–1, 2021.
- [15] S. Cetin, A. Demir, A. Yezzi, M. Degertekin, and G. Unal, "Vessel tractography using an intensity based tensor model with branch detection," *IEEE Trans. Med. Imag.*, vol. 32, no. 2, pp. 348–363, 2013.
- [16] T. Jerman, F. Pernuš, B. Likar, and Ž. Špiclin, "Beyond frangi: an improved multiscale vesselness filter," in *Proc. SPIE*, vol. 9413, 2015.
- [17] Y. Chi, J. Liu, S. K. Venkatesh, S. Huang, J. Zhou, Q. Tian, and W. L. Nowinski, "Segmentation of liver vasculature from contrast enhanced CT images using context-based voting," *IEEE Trans. Biomed. Eng.*, vol. 58, no. 8, pp. 2144–2153, 2011.
- [18] S. Esneault, C. Lafon, and J.-L. Dillenseger, "Liver vessels segmentation using a hybrid geometrical moments/graph cuts method," *IEEE Trans. Biomed. Eng.*, vol. 57, no. 2, pp. 276–283, 2010.

- [19] G. Hamarneh and P. Jassi, "Vascusynth: Simulating vascular trees for generating volumetric image data with ground-truth segmentation and tree analysis," *Computerized medical imaging and graphics*, vol. 34, no. 8, pp. 605–616, 2010.
- [20] Z. Liu, Z. Wu, T. Li, J. Li, and C. Shen, "Gmm and cnn hybrid method for short utterance speaker recognition," *IEEE Transactions on Industrial Informatics*, vol. 14, no. 7, pp. 3244–3252, July 2018.
- [21] W. Dang, Z. Gao, L. Hou, D. Lv, S. Qiu, and G. Chen, "A novel deep learning framework for industrial multiphase flow characterization," *IEEE Transactions on Industrial Informatics*, pp. 1–1, 2019.
- [22] S. Lu, J. Feng, H. Zhang, J. Liu, and Z. Wu, "An estimation method of defect size from mfl image using visual transformation convolutional neural network," *IEEE Transactions on Industrial Informatics*, vol. 15, no. 1, pp. 213–224, Jan 2019.
- [23] T. Kitrungrotsakul, X.-H. Han, Y. Iwamoto, L. Lin, A. H. Foruzan, W. Xiong, and Y.-W. Chen, "Vesselnet: A deep convolutional neural network with multi pathways for robust hepatic vessel segmentation," *Computerized Medical Imaging and Graphics*, vol. 75, pp. 74 – 83, 2019. [Online]. Available: <http://www.sciencedirect.com/science/article/pii/S0895611118304099>
- [24] A. Nazir, M. N. Cheema, B. Sheng, H. Li, P. Li, P. Yang, Y. Jung, J. Qin, J. Kim, and D. D. Feng, "Off-enet: An optimally fused fully end-to-end network for automatic dense volumetric 3d intracranial blood vessels segmentation," *IEEE Transactions on Image Processing*, vol. 29, pp. 7192–7202, 2020.
- [25] A. Nazir, M. N. Cheema, B. Sheng, P. Li, H. Li, P. Yang, Y. Jung, J. Qin, and D. D. Feng, "Spst-cnn: Spatial pyramid based searching and tagging of livers intraoperative live views via cnn for minimal invasive surgery," *Journal of Biomedical Informatics*, vol. 106, p. 103430, 2020. [Online]. Available: <http://www.sciencedirect.com/science/article/pii/S1532046420300587>
- [26] Ö. Çiçek, A. Abdulkadir, S. S. Lienkamp, T. Brox, and O. Ronneberger, "3D U-Net: Learning dense volumetric segmentation from sparse annotation," in *MICCAI*, 2016, pp. 424–432.
- [27] Z. Abderrahmane, G. Ganesh, A. Crosnier, and A. Cherubini, "A deep learning framework for tactile recognition of known as well as novel objects," *IEEE Transactions on Industrial Informatics*, pp. 1–1, 2019.
- [28] M. N. Cheema, A. Nazir, B. Sheng, P. Li, J. Qin, and D. D. Feng, "Liver extraction using residual convolution neural networks from low-dose CT images," *IEEE Trans. Biomed. Eng.*, pp. 1–10, 2019.
- [29] M. N. Cheema, A. Nazir, B. Sheng, P. Li, J. Qin, J. Kim, and D. D. Feng, "Image-aligned dynamic liver reconstruction using intra-operative field of views for minimal invasive surgery," *IEEE Trans. Biomed. Eng.*, pp. 1–11, 2018.
- [30] G. Wang and J. Qi, "PET image reconstruction using kernel method," *IEEE Trans. Med. Imag.*, vol. 34, no. 1, pp. 61–71, 2015.
- [31] Y. zhan Zeng, S. hui Liao, P. Tang, Y. qian Zhao, M. Liao, Y. Chen, and Y. xiong Liang, "Automatic liver vessel segmentation using 3d region growing and hybrid active contour model," *Computers in Biology and Medicine*, vol. 97, pp. 63 – 73, 2018. [Online]. Available: <http://www.sciencedirect.com/science/article/pii/S0010482518300957>
- [32] R. Zhang, Z. Zhou, W. Wu, C.-C. Lin, P.-H. Tsui, and S. Wu, "An improved fuzzy connectedness method for automatic three-dimensional liver vessel segmentation in ct images," *Journal of Healthcare Engineering*, vol. 2018, 2018.
- [33] L. Bi, J. Kim, A. Kumar, D. Feng, and M. Fulham, "Synthesis of positron emission tomography (pet) images via multi-channel generative adversarial networks (gans)," in *Molecular Imaging, Reconstruction and Analysis of Moving Body Organs, and Stroke Imaging and Treatment*, M. J. Cardoso, T. Arbel, F. Gao, B. Kainz, T. van Walsum, K. Shi, K. K. Bhatia, R. Peter, T. Vercauteren, M. Reyes, A. Dalca, R. Wiest, W. Niessen, and B. J. Emmer, Eds. Cham: Springer International Publishing, 2017, pp. 43–51.
- [34] J. Hoffman, E. Tzeng, T. Park, J. Zhu, P. Isola, K. Saenko, A. A. Efros, and T. Darrell, "Cycada: Cycle-consistent adversarial domain adaptation," *CoRR*, vol. abs/1711.03213, 2017. [Online]. Available: <http://arxiv.org/abs/1711.03213>
- [35] A. Radford, L. Metz, and S. Chintala, "Unsupervised representation learning with deep convolutional generative adversarial networks," 2015, cite arxiv:1511.06434Comment: Under review as a conference paper at ICLR 2016. [Online]. Available: <http://arxiv.org/abs/1511.06434>
- [36] C. Lin, E. Yumer, O. Wang, E. Shechtman, and S. Lucey, "ST-GAN: spatial transformer generative adversarial networks for image compositing," *CoRR*, vol. abs/1803.01837, 2018. [Online]. Available: <http://arxiv.org/abs/1803.01837>
- [37] I. Polycarpou, G. Soutanidis, and C. Tsoumpas, "Synthesis of realistic simultaneous positron emission tomography and magnetic resonance imaging data," *IEEE Trans. Med. Imag.*, vol. 37, no. 3, pp. 703–711, 2018.
- [38] T. Kim, M. Cha, H. Kim, J. K. Lee, and J. Kim, "Learning to discover cross-domain relations with generative adversarial networks," *CoRR*, vol. abs/1703.05192, 2017. [Online]. Available: <http://arxiv.org/abs/1703.05192>
- [39] Y. Cao, L. Jia, Y. Chen, N. Lin, C. Yang, B. Zhang, Z. Liu, X. Li, and H. Dai, "Recent advances of generative adversarial networks in computer vision," *IEEE Access*, vol. 7, pp. 14 985–15 006, 2019.
- [40] P. Isola, J. Zhu, T. Zhou, and A. A. Efros, "Image-to-image translation with conditional adversarial networks," in *2017 IEEE Conference on Computer Vision and Pattern Recognition (CVPR)*, 2017, pp. 5967–5976.
- [41] P. Isola, J.-Y. Zhu, T. Zhou, and A. A. Efros, "Image-to-image translation with conditional adversarial networks," in *IEEE CVPR*, 2017, pp. 5967–5976.
- [42] P. Costa, A. Galdran, M. I. Meyer, M. Niemeijer, M. Abramoff, A. M. Mendonça, and A. Campilho, "End-to-end adversarial retinal image synthesis," *IEEE Trans. Med. Imag.*, vol. 37, no. 3, pp. 781–791, 2018.
- [43] Y.-z. Zeng, Y.-q. Zhao, P. Tang, M. Liao, Y.-x. Liang, S.-h. Liao, and B.-j. Zou, "Liver vessel segmentation and identification based on oriented flux symmetry and graph cuts," *Computer Methods and Programs in Biomedicine*, vol. 150, pp. 31–39, 2017.